

<https://doi.org/10.1038/s41528-024-00310-6>

# Kirigami-inspired, three-dimensional piezoelectric pressure sensors assembled by compressive buckling

Check for updates

Yi Zhang<sup>1,2</sup>, Changbo Liu<sup>2,3</sup>✉, Ben Jia<sup>2,3</sup>, Dongqin Ma<sup>2,3</sup>, Xuecheng Tian<sup>1,2</sup>, Yuanyuan Cui<sup>1,2</sup> & Yuan Deng<sup>1,2</sup>✉

Piezoelectric sensors whose sensing performances can be flexibly regulated hold significant promise for efficient signal-acquisition applications in the healthcare field. The existing methods for regulating the properties of polyvinylidene fluoride (PVDF) films mainly include material modification and structural design. Compared to material modification, which has a long test period and an unstable preparation process, structural design is a more efficient method. The kirigami structure combined with compressive buckling can endow the flexible film with rich macrostructural features. Here, a method is fabricated to modulate the sensing performance by employing distinct 3D structures and encapsulation materials with varying Young's moduli. The relationship among the aspect ratio ( $\alpha$ ), pattern factor ( $\eta$ ), elastic modulus of encapsulation materials, and equivalent stiffness is obtained by finite element simulation, which provides theoretical guidance for the design of the 2D precursor and the selection of encapsulation materials. In the demonstration applications, the sensor accurately captures pulse waveforms in multiple parts of the human body and is employed for the pressure monitoring of different parts of the sole under various posture states. This method of structure design is efficient, and the preparation process is convenient, providing a strategy for the performance control of piezoelectric pressure sensors.

Advanced piezoelectric pressure sensors play a pivotal role in the field of healthcare monitoring, encompassing critical applications such as blood pressure measurement<sup>1</sup>, plantar-pressure analysis<sup>2</sup>, respiratory monitoring<sup>3</sup>, human-motion detection<sup>4</sup>, and human-speech recognition<sup>5</sup>. This is attributed to their fast response<sup>6</sup>, wide measuring range<sup>7</sup>, compact size<sup>8</sup> and easy fabrication<sup>9</sup>. Due to their elevated piezoelectric coefficient, which can reach up to  $1500 \text{ pC N}^{-1}$ <sup>10</sup> and far exceeds those of other piezoelectric materials<sup>11–13</sup>, piezoelectric ceramics have been extensively utilized in the manufacture of pressure sensors. However, they cannot bend and stretch because of their high stiffness and density values, limiting their application in healthcare monitoring. They also exhibit a high acoustic impedance, which hinders the effective conversion between mechanical and electrical energy. In contrast, piezoelectric polymers exhibit exceptional flexibility and an acoustic impedance closely matching that of the human body. Among them, polyvinylidene fluoride (PVDF) exhibits a high sensitivity, and its impedance is compatible with the human skin. Thus, it has

become one of the most employed materials for flexible, wearable pressure-sensing equipment<sup>14–19</sup> and has shown significant application potential in human-machine interfaces<sup>20</sup>, pulse signal acquisition<sup>21–24</sup>, flexible electronic skin<sup>25–27</sup>, energy collection<sup>28–31</sup> and other fields.

However, the low piezoelectric coefficient of PVDF restricts its performance in pressure sensors. In particular, for faint physiological signals, PVDF-based pressure sensors frequently struggle to achieve precise capture, and they present significant measurement errors in the presence of environmental interference<sup>32,33</sup>. In human signal monitoring, sensors are expected to be portable, exhibit excellent linearity, and possess high flexibility<sup>34</sup>. In this regard, straightforward signal-processing circuits have been demonstrated to meet these requirements, and the resulting sensors can withstand varying degrees of deformation. Nevertheless, the acquisition of different signals imposes distinct performance-attribute requirements on pressure sensors. For instance, the typical plantar pressure is  $1900 \text{ kPa}$ <sup>34</sup>, and the reported upper limit is  $3 \text{ MPa}$ <sup>35</sup>. In contrast, sensors employed for

<sup>1</sup>Research Institute for Frontier Science, Beihang University, Beijing 100191, China. <sup>2</sup>Key Laboratory of Intelligent Sensing Materials and Chip Integration Technology of Zhejiang Province, Hangzhou Innovation Institute of Beihang University, Hangzhou 310051, China. <sup>3</sup>School of Materials Science and Engineering, Beihang University, Beijing 100191, China. ✉e-mail: [liuchb@buaa.edu.cn](mailto:liuchb@buaa.edu.cn); [dengyuan@buaa.edu.cn](mailto:dengyuan@buaa.edu.cn)

pulse-signal measurement have a maximum detection limit of 500 Pa<sup>36</sup>. Given the substantial force exerted by the plantar pressure, it becomes imperative for pulse sensors to maintain a significant output voltage even under minimal pressure. Moreover, the presence of high cyclic loads may lead to deformation or fatigue<sup>37</sup>, emphasizing the importance of sensor stability during prolonged foot-pressure measurements. Therefore, flexible performance adjustments are vital to cater to diverse application scenarios.

Currently, the performance modulation of PVDF piezoelectric films primarily relies on material modification methods<sup>38–41</sup>, such as adding nanofillers (NaNbO<sub>3</sub> and RGO)<sup>42</sup>, doping MXene and BaTiO<sub>3</sub><sup>7</sup>, or preparing PVDF/ZnO nanofibers<sup>43</sup>. These methods involve extended development cycles and involve complex fabrication processes<sup>44,45</sup>. Structural design is another effective way to alter PVDF sensor performance. For instance, the microstructural design of materials can enhance sensor performance<sup>46,47</sup>. However, its impact remains constrained, and the structural formation remains intricate.

As a traditional artistic processing technique, kirigami introduces macroscopic changes to materials beyond their inherent elasticity by guiding deformation from two to three dimensions. When combined with compressive buckling, kirigami can generate various intriguing structures. The 3D kirigami structure is primarily influenced by the shape of the 2D planar precursor, and the cutting pattern is pivotal to the structural design. For 3D, kirigami-structured piezoelectric sensors, most reported applications involve cutting a planar PVDF film to construct a tensile structure<sup>48–50</sup>, with highly controllable tensile properties. However, the deformation is mostly confined within the plane, and the variety of pattern designs is not extensive, lacking development potential. In reality, strategically designed geometries and cutting patterns enable the assembly of 2D films into 3D kirigami structures, offering far greater applicability and topological complexity compared with other methods<sup>51</sup>. For example, piezoelectric microsystems with intricate 3D frameworks exhibit excellent mechanical properties and functional capabilities<sup>52</sup>. Electronic devices with multilayer cage-like structures demonstrate excellent collapse resistance and can dynamically transmit compression force and temperature<sup>53</sup>.

Here, we develop a piezoelectric pressure sensor featuring 3D kirigami structures. Sensors with distinct structures, designed using simple geometric shapes, exhibit varying sensitivities and different output voltages. Differing from prior investigations on 3D flexible electronic devices, our study combines experimental testing with finite element analysis to explore the impact of 3D structural design and encapsulation materials on the sensitivity and output voltage of PVDF-based piezoelectric pressure devices. Additionally, the finite element model that successfully predicts the 3D shape and output performance. Sensors equipped with 3D kirigami structures find application in human-pulse-signal and plantar-pressure measurements, showcasing exceptional operational stability under prolonged pressure conditions. This study introduces efficient 3D design concepts for PVDF-based pressure sensors and presents strategies for tackling the challenges associated with flexible, wearable pressure sensors.

## Results and discussions

### Fabrication of the 3D-structured piezoelectric pressure sensor

The fabrication process of the piezoelectric pressure sensor with a 3D kirigami structure is illustrated in Fig. 1a, and photos of the 3D kirigami-structured PVDF and the tensile platform are provided in Supplementary Fig. 1a. Femtosecond laser milling is utilized for the high-precision patterning of the PVDF film coated with a silver electrode layer. The optical image of the patterned piezoelectric film is shown in Supplementary Fig. 1b, with the edges of the 2D precursor retaining four symmetric anchor points to facilitate the 3D shaping process. The reserved four anchor points are mechanically affixed to a prestretched elastic substrate, which is subsequently uniformly relaxed to achieve the 3D structure. Releasing the pre-strain generates compressive forces, causing all regions, except the anchored areas, to bend out of the plane. Intermediate shapes corresponding to different levels of released prestrains are shown in Supplementary Fig. 2. The strain within the thin-film concentrates in the out-of-plane bending regions,

increasing as the degree of released prestrain increases. The phenomenon of charge cancelation is inevitable in the process of film compression and tension. This is mainly due to the negative deformation tendency of 3D structures caused by improper graphic design. We minimize intuitive canceling deformations through graphic design, which significantly reduces charge cancelation and ensures efficient sensor output. The device fabrication is finalized by pouring a silicone elastic encapsulation material (Ecoflex™ 00-10), which is employed to protect the PVDF film from moisture and harmful contaminants and provide deformation recovery capability.

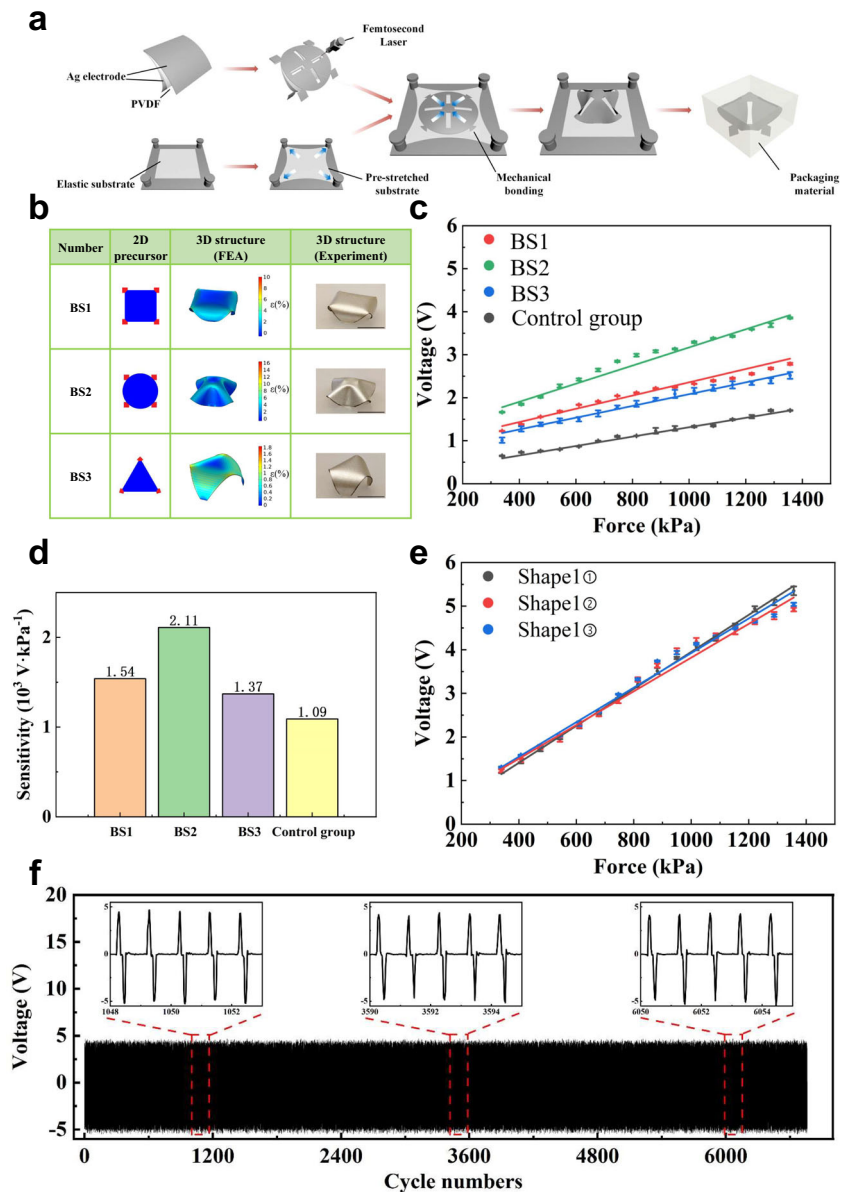
The basic shape of the 2D precursor determines the shape of the 3D structure. In this work, the 2D basic shapes, square, circle, and triangle, are designed with the same area as the basis (the corresponding samples are named BS1, BS2, and BS3). The structural images of the above three 3D kirigami structures are depicted in Fig. 1b. Finite Element Analysis (FEA) indicates that different basic shapes correspond to different maximum principal strain limits, with BS2 having the maximum value and BS3 having the minimum. When external pressure within the range of approximately 300–1,400 kPa is vertically applied to the sensors, their open-circuit voltage changes approximately linearly, as shown in Fig. 1c. The sensitivity of the three sensors (shown in Fig. 1d) are significantly higher than those of the control group. In comparison with the control group, the BS2 sample, featuring 2D circular precursors, offers more than a double increase in sensitivity and output voltage at the same pressure. The 3D structural diagram in the finite element analysis shows that the sensor with a 3D structure has a larger strain than the planar structure (control group, with zero strain). Consequently, it has better sensitivity and output voltage than the control group. The maximum principal strain of BS2 is greater than those of BS1 and BS3. The 3D-formed film has higher strains at the bending points, and due to the curved boundaries, BS2 has more significant strain areas. The larger strain generated during 3D forming improves the deformation capability of BS2, resulting in the highest output among all samples. Additionally, when conducting measurements exceeding 100 instances, we observe a very small margin of error. In this context, the output of the sensor can be significantly improved through 3D kirigami structural design, and further optimization of the 2D pattern can adjust the sensor's performance.

To verify the repeatability of the fabrication process of the 3D kirigami-structured sensor, we prepare three sensors with the same structure (Shape 1 shown in Fig. 2a). The performance test results are shown in Fig. 1e, where the three sensors exhibit comparable output voltages with sensitivity differences within 5%. This indicates the high repeatability of the fabrication process. As depicted in Fig. 1f, the output voltage remains stable after 6,000 pressurization release cycles of the 3D kirigami-structured sensor (Shape 1) with a pressure of 1,356 kPa. The proposed piezoelectric pressure sensor, which has a 3D structure, exhibits excellent operational stability.

### Sensor designs with various shapes and patterns

To investigate the influence of kirigami patterns on the device output performance, various kirigami patterns based on a circular shape are fabricated, whose performances are superior to those of the patterns based on square and triangular shapes, as illustrated in Fig. 2a. Here, four different shapes are designed and named as Shape 1, Shape 2, Shape 3, and Shape 2s. Different shapes result in distinct 3D kirigami structures, with Shape 1 forming a pyramid-like structure. Among the four different shapes, the cutting-damage percentages for Shape 1, Shape 3, and Shape 2s are approximately 12%. Under the same pattern as Shape 2, the cutting-damage percentage for Shape 2 is approximately 50%. Figure 2a shows that the different 3D structures exhibit varying levels of deformation at the same compression-buckling degree. Despite the pressure being applied vertically above the device, the encapsulation material envelops the film with a 3D structure, and the film structures have gradually increasing radii from top to bottom. Therefore, the vertically applied pressure extrudes the encapsulation material below, causing outward compression. The sensor deformation gradually reduces the out-of-plane dimensions and increases the in-plane dimensions until the structure becomes planar.

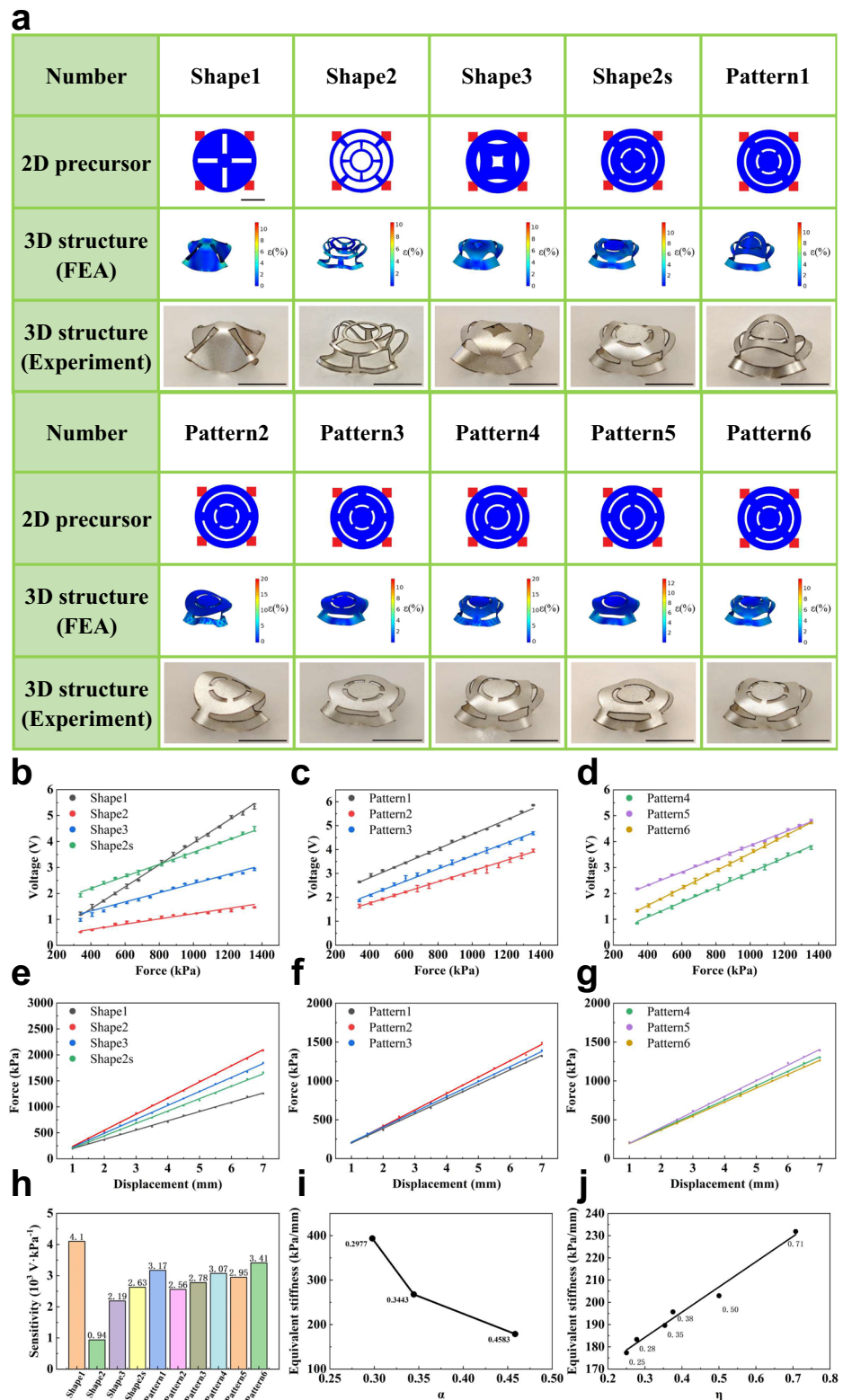
**Fig. 1 | Piezoelectric pressure sensor with 3D structures.** **a** Fabrication process of the 3D-structured piezoelectric pressure sensors on the prestrain forming. **b** Two-dimensional precursors, optical images, and FEA predictions for three basic shapes: square, circular, and triangular (scale bars: 5 mm). **c** Variation in the open-circuit voltage with different forces for the three stereoscopic and control groups (planar structures). **d** Sensitivity of the three stereoscopic and control groups (planar structures). **e** Variation in the open-circuit voltage with different forces for the three samples with the same structure (Shape 1). **f** Variation in the voltage of the pressure sensor with Shape1 after 6000 pressurization/release cycles at 1356 kPa.



As shown in Fig. 2b, with the same pattern elements, Shape 2s provides an output voltage of over 4 V at the maximum pressure, whereas Shape 2 only provides about 1 V. This indicates that the effective area of the film directly influences the signal output and sensitivity. The smaller the area of the film involved in the deformation, the lower the output voltage under the same pressure. The sensitivities of the four structures are  $4.1 \times 10^3 \text{ V kPa}^{-1}$  (Shape 1),  $0.94 \times 10^3 \text{ V kPa}^{-1}$  (Shape 2),  $2.19 \times 10^3 \text{ V kPa}^{-1}$  (Shape 3), and  $2.63 \times 10^3 \text{ V kPa}^{-1}$  (Shape 2s), respectively. Among Shape 1, Shape 3, and Shape 2s with similar cutting-damage percentages, Shape 1 exhibits the highest sensitivity. Initially, only the small top area of the film deforms when pressure is applied. Thus, the output voltage of Shape 1 is smaller than that of Shape 2s. As a larger area of the film participates in deformation, the structural advantage of a larger  $\alpha$  value gives Shape 1 the highest sensitivity. The 3D structure of Shape 3 is similar to that of Shape 2s, resulting in similar sensitivity values. However, Shape 2s has longer cutting lines, which allows for a larger number of narrower, free-bending strip elements given the same cutting area. Shape 2s has a larger  $\alpha$  value, leading to a higher output voltage compared with Shape 3. Shape 3 and Shape 2s exhibit similar sensitivities; however, their output voltages are 1.5 times different, confirming that the sensitivity and output voltage of the sensor can be adjusted by optimizing the pattern design.

Considering that besides the shape, the design details of the 2D precursor influence the sensor's performance, six different kirigami patterns based on Shape 2s are designed, and the corresponding 3D kirigami-structured sensors are fabricated. The 2D precursor designs, as well as the 3D structure in FEA and in the experiment, are shown in Fig. 2a. In the six patterns of the 2D precursor designs, as shown in Fig. 2a, the internal cutting patterns of Patterns 1–3 are similar, whereas the external cutting lines of Pattern 1 and Pattern 2 are rotated  $45^\circ$  relative to each other. The number of outer cutting lines of Pattern 3 increases from two to four, compared with that for Pattern 2. The cutting patterns of Pattern 4 and Pattern 5 are basically similar, except that the pattern is rotated  $45^\circ$  relative to the anchor point. The difference between pattern 6 and pattern 4 is that the former has four cut lines inside. As shown in Fig. 2c, Pattern 1, Pattern 2, and Pattern 3 exhibit sensitivities of  $3.17 \times 10^3$ ,  $2.56 \times 10^3$ , and  $2.78 \times 10^3 \text{ V kPa}^{-1}$ , respectively. Pattern 1 also exhibits the highest output voltage in the full test-pressure range as well as the highest sensitivity, whereas Pattern 2 exhibits the lowest values in the above two properties. The sensitivities of Pattern 4, Pattern 5, and Pattern 6 are  $3.07 \times 10^3$ ,  $2.95 \times 10^3$ , and  $3.41 \times 10^3 \text{ V kPa}^{-1}$ , respectively, as presented in Fig. 2d. Although the output voltages of Pattern 5 and Pattern 6 are similar, the sensitivity of Pattern 6 is higher than that of Pattern 5. The sensitivity of Pattern 4 is similar to that of Pattern 5, and

**Fig. 2 | Designs with various shapes and patterns of the piezoelectric pressure sensor.** **a** Two-dimensional precursors, photographs, and FEA predictions for four different shapes and six similar patterns (scale bars: 5 mm). Variation in the open-circuit voltage with different forces for **(b)** Shape 1, Shape 2, Shape 3, and Shape 2s; **(c)** Pattern 1, Pattern 2, and Pattern 3; and **(d)** Pattern 4, Pattern 5, and Pattern 6 in the experiment. Variation in the force with different displacements for **(e)** Shape 1, Shape 2, Shape 3, and Shape 2s; **(f)** Pattern 1, Pattern 2, and Pattern 3; and **(g)** Pattern 4, Pattern 5, and Pattern 6 in FEA. **h** Sensitivity of the 3D structure formed by four shapes and six patterns structures. **i** Variation in the equivalent stiffness with different  $\alpha$  values based on three sensors with various shapes. **j** Variation in the equivalent stiffness with different  $\eta$  based on six sensors with various patterns.



Pattern 4 exhibits the lowest output voltage. The sensors fabricated based on different patterns exhibit significant variations in performance, suggesting that even subtle changes in patterns can influence sensor performance. Further research is required to explore the underlying reasons.

To explore the factors that affect the sensitivity and output voltage of the sensors, a finite element simulation model is established according to the test environment in the experiment. Since the deformation of the sensor during the compression process is relatively complex, the compression

displacement in the direction perpendicular to the bottom surface is adopted to describe the deformation degree of the sensor. The equivalent stiffness is employed to evaluate the deformation capability of the sensor, which is defined as the ratio of the external load on the sensor to the compression length of the sensor in the vertical direction. FEA reveals that with the increase in pressure, the vertical compression displacement linearly increases. The correlation between pressure and compression displacement of the four shapes and Patterns 1–6 is shown in Fig. 2e–g, where the



compression displacement varies from 1 to 7 mm, and the height of the sensor is 10 mm. The sensitivity of the 3D structure formed by four shapes and six patterns structures is shown in Fig. 2h. To illustrate the impact of different shapes on the sensor's performance, the 3D extension among various shapes is defined using the aspect ratio ( $\alpha$ ) expressed as follows:

$$\alpha = d_{\text{out}}/d_{\text{in}} \quad (1)$$

where  $d_{\text{out}}$  and  $d_{\text{in}}$  are defined as the maximum out-of-plane dimension and in-plane extent, respectively (see Supplementary Fig. 3a and b). The  $\alpha$  value of Shape 1 is 0.4583, whereas that of Shape 2s is 0.3443, which is larger than that of Shape 3 (0.2977). This indicates that the performance of the sensor increase with the increase in the 3D extension. For Shape 1, Shape 3, and Shape 2s, when the packaging material is the same, the relationship between the  $\alpha$  value and the equivalent stiffness is shown in Fig. 2i. With the increase in the effective stiffness, the  $\alpha$  value decreases, which indicates that the extension size of the 3D structure affects the deformation ability to a certain extent. Although Patterns 1–6 have the same shape and similar  $\alpha$  values, their performances differ, indicating that factors other than the  $\alpha$  value influence their sensitivity and output voltage. Since laser cutting generates a hinged circular structure with a radius from the connecting point to the central point, the outer and inner beams are defined as the connecting points between the rings in the pattern, which provides support for the 3D structure, as shown in Supplementary Fig. 3c.  $\text{Angle}_1$  is the angle between the anchor point (red region) and the outer beam, and  $\text{Angle}_2$  is the angle between the outer beam and the inner beam; the relationship between them and the equivalent stiffness under different patterns are shown in Supplementary Fig. 3d. To ensure symmetry in the 3D structures, all the included angles are only set to  $0^\circ$  or  $45^\circ$ . In the three patterns with the smallest equivalent stiffness values, the two angles are  $0^\circ$ . In addition to the values of the included angles, the number of angles also affects the deformation characteristics of the structure. Here,  $\eta$  is defined as a pattern factor that represents the effect of the magnitude and the numbers of the two types of angles in the 2D design pattern:

$$1/\eta = 2/3 \times n_1 \times \cos(\text{Angle}_1) + 1/3 \times n_2 \times \cos(\text{Angle}_2) \quad (2)$$

where  $n_1$  and  $n_2$  are the numbers of the outer and inner beams, respectively, and “2/3” indicates that the ratio of the outer to the inner area is 3:2. Due to symmetry, the angle is set to  $0^\circ$  and  $45^\circ$ , so the components in the formula related to the angle should be cosine values. Since there are two types of beams, their quantity should be a product of cosine values. Additionally, considering the difference in the area of the inner and outer sides of the beam, the pattern factor's components' weights are determined based on the ratio of the areas. Due to symmetry, the angle is set to  $0^\circ$  and  $45^\circ$ , so the components in the formula related to the angle should be cosine values. Since there are two types of beams, their quantity should be a product of cosine values. Additionally, considering the difference in the area of the inner and outer sides of the beam, the pattern factor's components' weights are determined based on the ratio of the areas. The variation in the  $\eta$  value with different equivalent stiffness values based on the six sensors with various patterns is depicted in Fig. 2j. The  $\eta$  value increases linearly with the equivalent stiffness, indicating that when the number of beams reaches the maximum and the angle between the beam and the anchor point on the line is  $0^\circ$ , the equivalent stiffness is the lowest. In other words, the smaller the  $\eta$  value, the stronger the deformation ability of the corresponding 3D structure. This can play a guiding role in the graphic design of the 2D precursor of the piezoelectric pressure sensor with such a 3D structure: the basic shape is circular, and the number of supporting beams, as well as the angle between them and the anchor point, is supposed to be prioritized while maximizing the aspect ratio. Furthermore, to validate the effectiveness of FEA, the output performances of the 10 sensors shown in Fig. 2a are computed using a finite element model, and the results are presented in Supplementary Figs. 4a and 4b. Evidently, the finite element model can accurately predict the sensor's output performance, although there is a slight deviation between

the simulated output voltage and the test data, as shown in Supplementary Fig. 4c. This discrepancy can be attributed to differences between the defined elastic material model and the actual material properties. The established FEA model holds significance in the design of 3D-structured sensors. As shown in Supplementary Fig. 4d, the sensor's performance is optimal when the two angles tend to  $0^\circ$ , as shown by the higher sensitivity values of Patterns 1 and 6. When the angles are consistent, the number of inner and outer beams also affects the sensor's output, with Pattern 6 having slightly higher sensitivity than Pattern 1 due to having more outer beams. Therefore, the angles and numbers of inner and outer beams jointly determine structural performance. For instance, the difference between Patterns 2 and 1 is reflected in the angle, and the difference between Patterns 2 and 3 is reflected in the number of outer beams. Besides, because the basic shape of the 2D precursor was circular, the cutting elements consist of arcs with the same radii, thus somewhat limiting the freedom of graphic design. In the future, various structural designs can be expanded by altering the radii and angles of the cutting elements, including the spacing between different cutting lines, based on symmetry. This approach will enable the exploration of factors with significant impacts on design, allowing for further typical and diverse design explorations.

### Sensor designs with various encapsulation materials

Notably, the deformation ability of the 3D-structured piezoelectric pressure sensors can be adjusted by changing the packaging material. Four types of silicone resin materials are used as encapsulation materials, with Young's moduli of 50, 170, 418, and 1,000 kPa, respectively. The results of the tensile tests are shown in Supplementary Fig. 5.

The test data are shown in Fig. 3a, b, and c. For Shape 1, the sensitivities of M1–M4 are  $4.1 \times 10^3$ ,  $3.15 \times 10^3$ ,  $1.73 \times 10^3$ , and  $1.35 \times 10^3$  V kPa<sup>-1</sup>, respectively. For sensors with three different 3D kirigami structures, as the Young modulus of the encapsulation material decreases, the output voltage increases under the same applied pressure, resulting in improved sensitivity. For instance, for Shape 1, when the pressure is approximately 1,300 kPa, the sensor encapsulated with M1 provides an output voltage of over 5 V, which is approximately 1.3, 2.2, and 2.7 times those of M2, M3, and M4, respectively. This indicates that the modulus of the encapsulation material significantly affects the performance of the sensor.

The relationship between the compression displacement and the applied pressure is shown in Fig. 3d–f. Similar to the previous case, a similar trend is observed for sensors prepared using different encapsulation materials. The vertical compression displacement shows a linear increase with the pressure, as confirmed by finite element simulation calculations. The relationship between Young's modulus and the equivalent stiffness of the encapsulation materials for the three structures is shown in Supplementary Fig. 6. FEA reveals that the equivalent stiffness exhibits a nonlinear variation with the changes in the Young modulus of the encapsulation material. Notably, when the Young's modulus falls within the range of 200–400 kPa, the equivalent stiffness experiences a significant increase. However, the variation in the equivalent stiffness is less pronounced beyond this range. This indicates that the performance of the sensor is sensitive to the Young modulus of the encapsulation material in the range of 200–400 kPa. When the pressure is 1000 kPa, the distribution of the maximum principal strain for various sensors in the FEA is illustrated in Fig. 3g. For Shape 1, as the Young modulus of the encapsulation material increases, the deformation of the sensor under the same pressure gradually reduces. The reduction in the sensor deformation leads to a decrease in the sensitivity and output voltage, which is evident in Fig. 3a–c.

The FEA results closely resemble the experimental findings, offering valuable insights for guiding sensor design and performance prediction. As a result of the limitations imposed by the pressure-generation system, the true detection limit of the sensor cannot be obtained. To address this, FEA is implemented to predict the measurement limits of the various sensors. In the FEA, as the loads increase, the pressure reaches a saturation state, and the output voltage follows suit. We use finite element simulation analysis to predict the force limit of packaging materials with larger Young's modulus

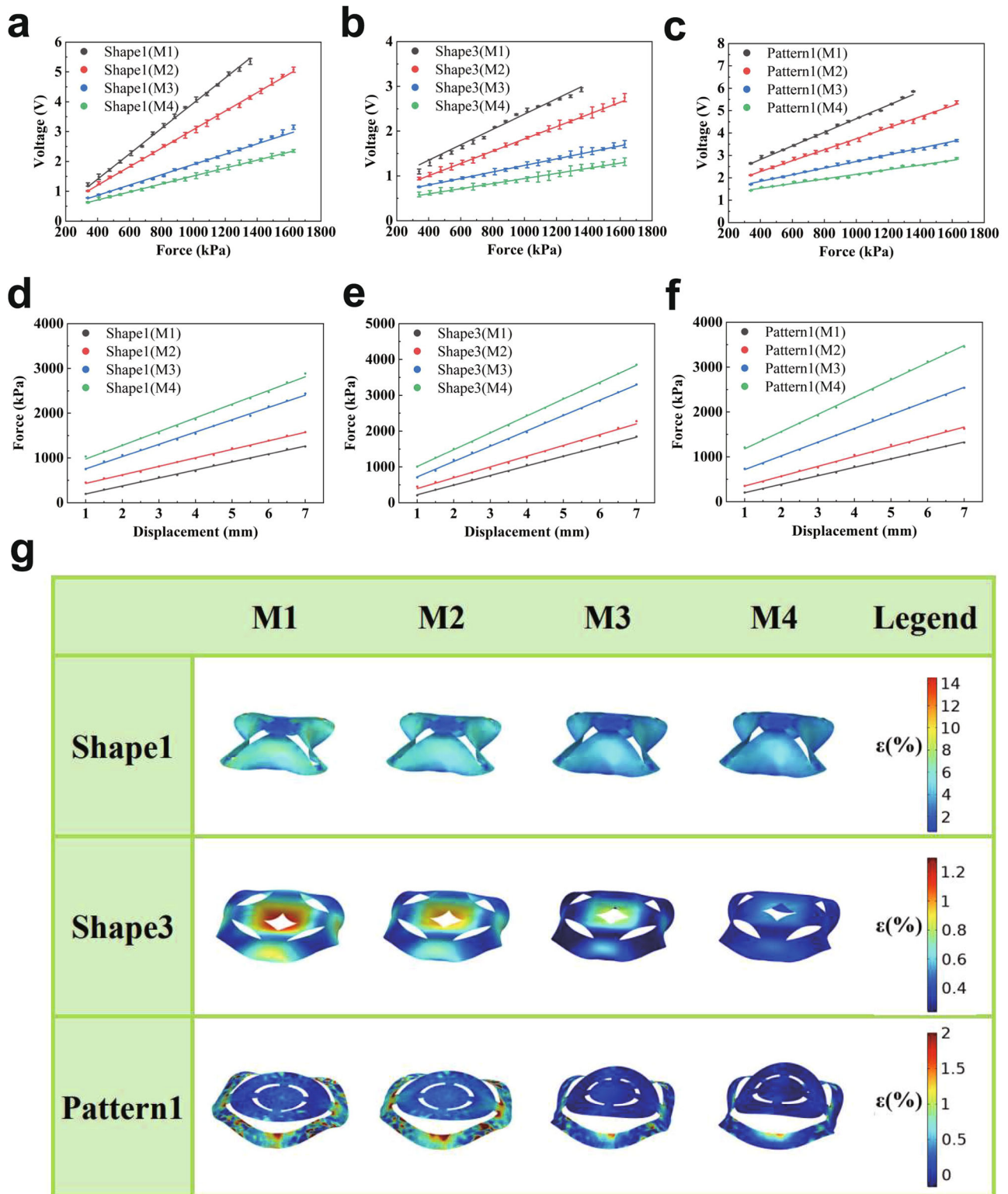


**Fig. 3 | Stress-test performance of the piezoelectric pressure sensors with different encapsulation materials.** Variation in the open-circuit voltage with different forces for (a) S1, (b) S3, and (c) P1 encapsulated with M1, M2, M3, and M4. Variation in the force with different displacements for (d) S1, (e) S3, and (f) P1

encapsulated with M1, M2, M3, and M4 in the FEA. **g** Strain distribution of the three sensors encapsulated with four materials under a pressure of 1000 kPa in the FEA. The colors in the FEA results correspond to the magnitudes of the maximum principal strain.

(2000 kPa and 5000 kPa). The maximum detection limits of each sensor predicted by FEA are shown in Supplementary Fig. 7. Additionally, when conducting measurements exceeding one hundred instances, we observe a very small margin of error. When the same encapsulation material is used,

the maximum detection limits of most structures are similar. With the increase in the Young's modulus, the maximum detection limit also increases, up to 4500 kPa, indicating that the measurement range of the sensor can be regulated by selecting appropriate encapsulation materials,

enabling flexible sensor-performance design. In practical applications, the choice of encapsulation material should be specific to the measurement range and environmental conditions. Simply reducing the stiffness of the encapsulation material can degrade the overall load-bearing capacity of the device, potentially resulting in delayed compression recovery or irreversible deformation. Small variations in pressure signals require devices with high sensitivity for accurate measurements. Although low stiffness of encapsulation materials may enhance measurement performance, it imposes high demands on the fabrication process, such as curing time and other conditions, thereby increasing production costs. Therefore, the selection of encapsulation materials should be tailored to different application scenarios. In previous studies, the sensitivity of kirigami-inspired pressure sensors varies greatly due to different materials and sensor structures, such as  $0.0051 \text{ V}\cdot\text{N}^{-1}$ <sup>49</sup>,  $0.067 \text{ V}\cdot\text{N}^{-1}$ <sup>39</sup>,  $0.060 \text{ V}\cdot\text{N}^{-1}$ <sup>52</sup>. Our study demonstrates that under the same material conditions, performance can be further enhanced through the design of kirigami structures. In our study, the sensitivity of the control group (planar PVDF film) is  $0.014 \text{ V}\cdot\text{N}^{-1}$ , and the sensitivity range that can be achieved via graphic regulation is  $0.025\text{--}0.056 \text{ V}\cdot\text{N}^{-1}$ .

### Pulse-signal measurement and motion-posture sensing

Pressure sensors play a very important role in health monitoring, and different application scenarios have different performance requirements for pressure sensors, such as pulse and foot-pressure monitoring. For the elderly population, pulse signals can serve as indicators of cardiovascular health<sup>54</sup>, and plantar pressure can be utilized to diagnose conditions, such as Parkinson's disease, diabetes, and stroke<sup>2</sup>.

The prepared sensors exhibit a high output voltage and sensitivity. They can be flexibly designed according to different needs and working conditions. To verify the application potential of the sensors in the field of health monitoring, pulse and plantar-pressure detection systems are developed based on the self-designed 3D kirigami structures. A series of sensors based on Shape 1 are fabricated, encapsulated with M1–M4, and integrated with a wristband to create a pulse detection system, as shown in Fig. 4a. Due to the large 3D structure, the sensor cannot be perfectly conformal with the skin, which brings discomfort to wear. However, comfort can be improved by designing smaller patterns, controlling pre-stretched base tension, and reducing sensor package thickness. In practical applications, the sensor can be installed in an upright or inverted orientation because the orientation does not affect its signal output, ensuring consistency in test results. The sensor is secured to the wrist using a wrist strap. Supplementary Fig. 8a shows the details of the sensor–skin contact interface. The pulse-signal detection performances of the sensors encapsulated with different materials are tested, as depicted in Fig. 4b. M1 exhibits the lowest Young's modulus, and its corresponding pulse-signal output voltage is the highest, exceeding  $0.2 \text{ V}$ , whereas M4 exhibits the lowest pulse-signal output voltage. The sensors fabricated with different encapsulation materials capture identical pulse details, including the length of the cardiac cycle and the temporal position of the tidal wave. This indicates that the signal output can be enhanced by selecting appropriate encapsulation materials, thereby improving the signal-to-noise ratio. To validate the reliability of the 3D sensor in wearable-device applications, we subject the sensors to simulated sweat-induced corrosion interference tests. Salt water with a mass fraction of 1% is employed to simulate the sweat, and the sensor is soaked for 96 h at  $37^\circ\text{C}$ . The pulse-test results before and after soaking are shown in Fig. 4c. After soaking, the performance of the sensor remains stable, and it retains its ability to accurately capture intricate pulse details. This is primarily attributed to the excellent hydrophobic properties of the encapsulation material employed. The difference in the waveform may be due to the changes in the physical state of the volunteer, which is also reflected in Fig. 4d. The pulse waveform exhibits noticeable changes in shape before and after exercises, the cardiac cycle is shortened, and the pulse-signal intensity is increased. In addition to the wrist, pulse-signal measurements are performed at four other locations using the prepared system, and the results are illustrated in Fig. 4e. The Shape 1 sensor encapsulated with M1 is employed to measure the pulse at the above positions simultaneously. The pulse waveform and intensity

vary significantly at different locations, with the highest pulse intensity observed at the carotid artery and the lowest at the ankle, which is consistent with the results obtained by normal finger touch. Although the measurement positions are different, the signal change cycle is the same, indicating that the signals measured in different parts are indeed human pulse signals. The shape and detailed parameters of the pulse signals from different locations correspond well to those reported in the literature, validating the measurement results<sup>55,56</sup>. This indicates that the sensor can detect physiological signals in multiple parts of the human body. Pulse signals at different positions are simultaneously monitored, and blood pressure information can be measured using the time difference. By simultaneously monitoring pulse signals at different positions, blood pressure information can be measured using the time difference. In the future, through integration with various external devices, sensors can be employed to monitor a broader range of physiological signals in the human body, such as blood pressure<sup>57</sup>, and respiratory rate<sup>58</sup>.

The variation in human plantar pressure is intricate, influenced by different motion states and various walking postures, leading to distinct pressures across different regions of the sole. Consequently, sensors with broad measurement ranges and high sensitivity are required. As depicted in Fig. 4f, the common plantar-pressure areas can be categorized into four types: the first, third, and fifth metatarsal heads, as well as the heel. As mentioned earlier, the sensing range and sensitivity of 3D kirigami-structured sensors can be dynamically tailored using different encapsulation materials and patterns, rendering them an ideal choice for plantar-pressure measurement. Therefore, based on this concept, a plantar-pressure-detection system is developed. In the plantar pressure monitoring, the subject's gravity was about  $740 \text{ N}$ , higher than the maximum pressure of about  $130 \text{ N}$  in the previous cycle test. However, the sensor does not undergo plastic deformation due to excessive pressure from the body weight. The robust mechanical performance of the sensor is due to the excellent elasticity of the encapsulation material, which allows the device to maintain stable compression and recovery under the weight of the human body, as shown in Supplementary Fig. 8b. We examine pressure variations in four different plantar regions for various posture states, as illustrated in Fig. 4g. In the tiptoeing state, the main force is the root of the first metatarsal bone. Owing to the slight contact between the heel and the ground, the sensor picks up a weak signal. In the walking and running states, the fifth metatarsal root is the most stressed, probably due to the certain degree of foot valgus. A good gait can help maintain normal posture while preventing muscle and joint strains. In particular, for patients who require rehabilitation exercise, the accurate detection of plantar pressure can help accelerate their recovery. The difference among waveforms can be exploited to distinguish different stress positions and motion states, which can be applied to the long-term monitoring of plantar pressure. To validate the sensor's performance under prolonged high-pressure conditions, a continuous running/jumping alternating test is conducted, with the sensor positioned at the base of the fifth metatarsal, as depicted in Fig. 4h. The sensor accurately captures walking signals even after multiple jumps, highlighting its high stability. This signifies the significant potential of the sensor in dynamically monitoring plantar pressure. The pulse signal and plantar pressure measurements showed that Shape 1, which performed best in the sensor performance characterization, was the best fit for the application. Through adjusting design patterns and altering encapsulation materials, flexible control of sensor performance can be achieved. These findings will enable the design of sensors for detecting signals of varying intensities, presenting significant prospects for applications in wearable devices and health monitoring.

In summary, we fabricate 3D, kirigami-structured pressure sensors based on PVDF piezoelectric thin films. By modifying the design of a 2D precursor and employing different encapsulation materials, the sensitivity and output voltage of the sensor could be flexibly adjusted. This method exhibits excellent reproducibility, resulting in flexible sensors with high mechanical durability. We also establish effective finite element models to guide the sensor design and predict the sensor's performance. Furthermore,



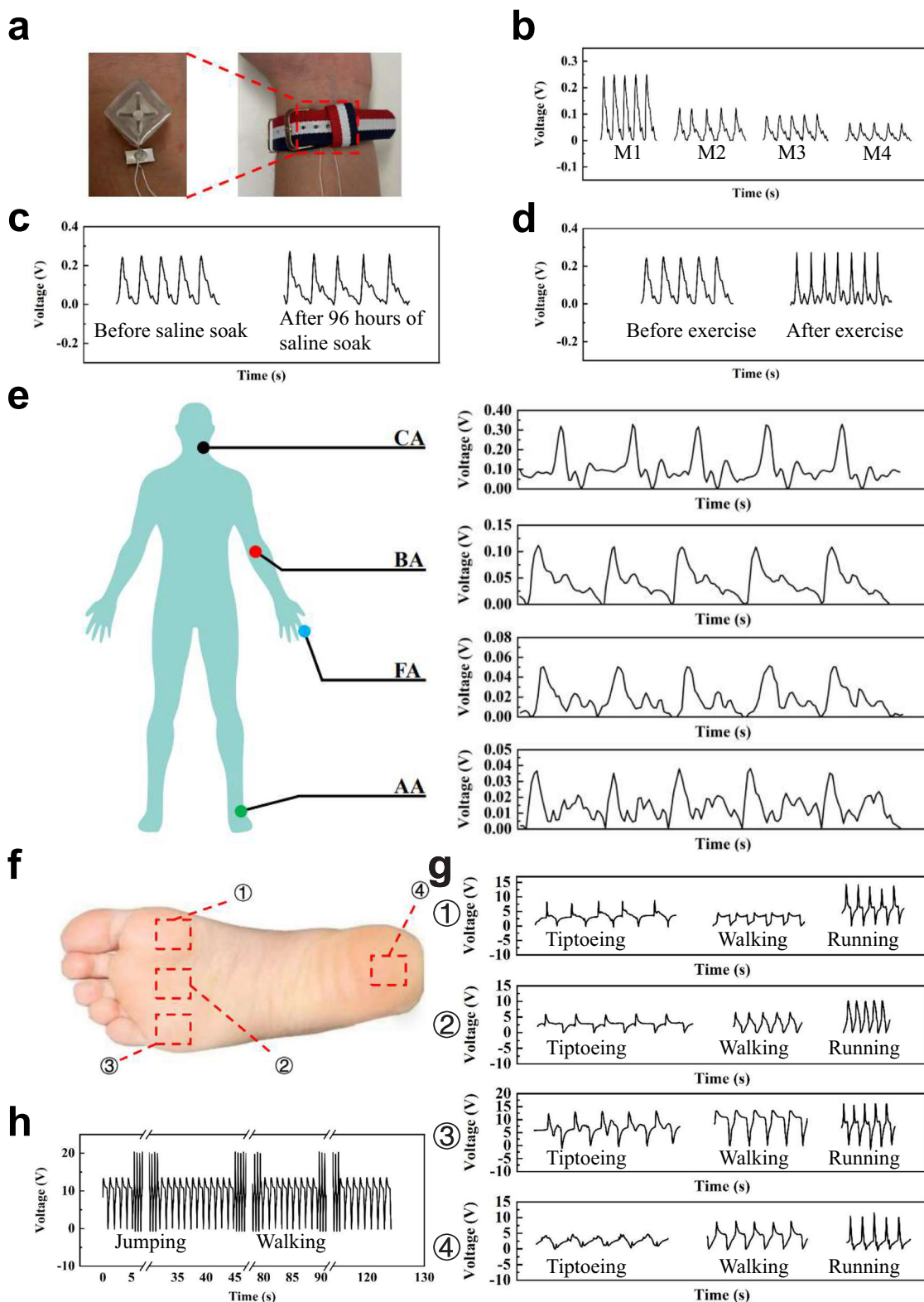


**Fig. 4 | Pulse-signal measurement and motion-posture sensing using the piezoelectric pressure sensor.** **a** Photograph of the P1 sensor conformally attached to the human wrist using an adjustable watchband. **b** Radial artery pulse signals detected by the P1 sensor encapsulated with four different materials. Pulse measurement before and after (c) sensor soak in saline and (d) exercise. **e** Pulse-signal measurement in

different parts of the human body. **f** Schematics of different plantar positions where the sensor is attached. **g** The open-circuit voltage of the P1 sensor attached to four different positions in tiptoeing, walking, and running states. **h** The open-circuit voltage of the P1 sensor placed at position ③ in alternating jumping/walking states.



our sensors successfully monitor both pulse signals and plantar pressure. In the future, more intriguing structural designs and superior encapsulation materials will be explored while further reducing the sensor size. In summary, this work provides a simple and effective approach for modulating the performance of piezoelectric pressure sensors. We anticipate that the macroscopic structural design of piezoelectric thin films would find broad application in various pressure-sensing devices.

## Methods

### Design of 2D precursors

Highly symmetric graphic designs are made for the 2D precursors to ensure the symmetry of the 3D structures and the stability of device operation. Squares and circles, representing classic shapes with straight and curved boundaries, respectively, exhibit different structural characteristics and distinct compression effects after formation. Both squares and circles have four anchor points and 90° angles. Additionally, triangles with three anchor points, each with angles of 120°, are considered basic shapes in the design. Drawing inspiration from common 3D structural elements in daily life, we devised a pyramid-like top-protruding (conical) structure (Shape 1), a concave-topped structure resembling an ancient Chinese coin (Shape 3), and three-layer disc-like structures (Shapes 2 and 2s). We kept the film area constant to investigate the impact of the structure as the sole variable on performance. The difference in cutting area between Shapes 2 and 2s was used to demonstrate the influence of the effective film area on the performance. Furthermore, for the same three-layer disc-like shape, given identical design elements for the 2D precursor, various interesting structures with the same planar shape but different pattern details can be created by changing the length and quantity of the cutting lines. We make further adjustments and create a second three-layer disc-like structure, Shape 2s, to obtain six different pattern designs.

### Fabrication of 3D structures

A PVDF film coated with electrodes (52 μm metallized piezo film, TE Connectivity) is patterned by Femtosecond laser (Pharos 20, Light Conversion) with a single-pulse energy of 2 mJ, a repetition frequency of 0.4 kHz, a processing speed of 150 mm s<sup>-1</sup>, and 200 processing cycles. The pre-designed 2D precursor design drawing (CAD data) and cutting parameters are input into the machining control system, and the machining process is automatically completed by the controller. Appropriate laser and cutting parameters can ensure effective cutting while the upper and lower electrode layers of the film are not conducting. The wires are connected in the rectangular region (Supplementary Fig. 1b) of the patterned film using conductive silver glue. At the same time, an elastic substrate with dimensions of 5×5 cm and thickness of 2 mm is fabricated by platinum-catalyzed silicones (Ecoflex™ 00-10, Smooth-On) in a 1:1 ratio under the condition of curing at 80°C for 30 minutes. The elastic substrate is then fixed on the manual tensile platform (PT-ST50, PDV, Supplementary Fig. 1a). The pre-strain of 130% is applied to the elastic substrate using tensile platforms. After the four anchor points are threaded through small holes at the target positions in the elastic substrate, the mechanical fixation of the anchor points is achieved by releasing the prestrain in the elastic substrate, thereby completing the formation of the 3D structure. As for lead wires, we cure the silver paste within the working temperature range of PVDF and then reinforce the connection points with the encapsulation material, ensuring electrode and conductor stability during testing and application. The image of the thin film section after laser cutting, which is shown in Supplementary Fig. 1c can show that the thin film does not short-circuit, which ensures the effectiveness of the voltage output.

### Packaging of piezoelectric pressure sensors

The elastic substrate is removed from the tensile platform after the 3D structure is formed. The mold is covered on the film with the 3D structure in order to control the shape of the sensor. The packaging material solution is then cast into the mold. The overall dimensions of the encapsulated sensor are 15 mm × 15 mm × 10 mm. A photo and cross-sectional image of the encapsulated device are shown in the Supplementary Fig. 1d and e. Here, four packaging materials, which include platinum-catalyzed silicones

(Ecoflex™ 00-10, Smooth-On) and three kinds of silicone materials (Sanjingxinde Technology) with different Young's moduli, are used to provide the sensor with deformation recovery capabilities. The Young's moduli of the packaging materials are 50 kPa, 170 kPa, 410 kPa and 1000 kPa respectively, which are tested by the intelligent electronic tensile testing machine (XLW-EC-A, Labthink). The stress-strain curves are shown in Supplementary Fig. 5. The curing condition is normal temperature curing. Mold and substrate removal are performed after the encapsulation material is cured. The encapsulation material wrapping ensures the stable compression and recovery of the 3D structure during operation after the removal of the substrate.

### Experimental setup for pressure and electrical characterization

The packaged sensor is placed on a fixed platform. The mechanical force perpendicular to the sensor's surface is provided using a strain system consisting of linear guides (H01, Linmot) and load cell (DYM103, DAYSENSOR) and is recorded by a high precision dynamometer (DY920, DAYSENSOR). The digit multimeter (Keithley 6500) is employed to capture and record the open-circuit voltage of the sensors. The pressure applied to the sensor surface varies with the moving distance of the linear guide. The absolute value of the open circuit voltage generates when the sensor is squeezed is recorded as the output voltage at that pressure. The force measuring device indicates that the sensor can detect forces as small as 0.1 N.

### Finite element analysis

The finite element analysis is performed using the Structural Mechanics and AC/DC modules of COMSOL Multiphysics. PVDF material parameters are subsequently configured. The PVDF material from the COMSOL material library is primarily utilized, with a Poisson's ratio set to 0.35 and a Young's modulus of 2600 MPa. Subsequently, the four anchor points are subjected to inward displacements of 2.8 mm along the x and y axes, respectively, simulating the film's contraction inward according to the length of contraction of the elastic substrate, ultimately forming a three-dimensional structure. Then a cuboid packaging material model with dimensions of 15 × 15 × 10 mm is created around the film to construct the sensor model. Simultaneously, a cuboid steel plate model is positioned above the sensor to mimic the pressure application device. For simulating the packaging material, the third-order superelastic material model Yeoh is chosen, and the parameters (c1, c2, and c3) correspond to the packaging Materials and are derived from the Soft Robotics Materials Database<sup>39</sup>. The material is considered incompressible. In the Electrical module, the upper surface voltage of the film is zero and the lower surface is grounded. In the Structural Mechanic module, the lower surface of the sensor model is kept moving freely in the lateral direction and constrained in the longitudinal direction. Meanwhile, the steel plate gradually moves downward, and its motion parameters are the same as those of the linear guide rail in the experiment, and are set as the acceleration, uniform speed and deceleration process, in which the acceleration and deceleration process are the same. Changes in strain distribution, pressure, and output voltage can be obtained by simulating the sensor compression process.

### Pulse signal detection

Radial pulse is measured by placing a sensor on the surface of the radial artery of the wrist and securing it with a watch strap. The pulse of the neck, fingertip, elbow and ankle is measured by placing the sensor in the designated position and fixing it in place with a band-aid. The pulse after exercise is measured after running lasts for 1 minute. The saline soak meant that the sensor is immersed in salt water with 1% at 37 °C. Pulse signals are collected using a shielded junction box (SCB-68A, National Instruments).

### Plantar pressure detection

The sensor secures using tape are placed at the heel and at the base of the first, third and fifth metatarsal bones on the sole of foot respectively. Tip-toeing meant that body weight is moving from the heel to the ball of the foot.

The difference between walking and running is the step frequency of the volunteers wearing the sensors, where the frequency is 1 Hz for walking and 3 Hz for running. Alternating jumping and running mean that the switch between jumping and running is quick. The wire of sensors is connected to the junction box of the shielding chamber and the open circuit voltage is recorded by the upper computer software.

### Data availability

All data needed to evaluate the conclusions in the paper are present in the paper and the Supplementary Information.

Received: 31 October 2023; Accepted: 29 March 2024;

Published online: 11 April 2024

### References

1. Yi, Z., Zhang, W. & Yang, B. Piezoelectric approaches for wearable continuous blood pressure monitoring: a review. *J. Micromech. Microeng.* **32**, 103003 (2022).
2. Chen, J.-L. et al. Plantar pressure-based insole gait monitoring techniques for diseases monitoring and analysis: A review. *Adv. Mater. Technol.* **7**, 2100566 (2022).
3. Chen, X. et al. Flexible fiber-based hybrid nanogenerator for biomechanical energy harvesting and physiological monitoring. *Nano Energy* **38**, 43–50 (2017).
4. Ghosh, S. K. & Mandal, D. Synergistically enhanced piezoelectric output in highly aligned 1D polymer nanofibers integrated all-fiber nanogenerator for wearable nano-tactile sensor. *Nano Energy* **53**, 245–257 (2018).
5. Guo, W. et al. Wireless piezoelectric devices based on electrospun PVDF/BaTiO<sub>3</sub> NW nanocomposite fibers for human motion monitoring. *Nanoscale* **10**, 17751–17760 (2018).
6. Dagdeviren, C. et al. Conformable amplified lead zirconate titanate sensors with enhanced piezoelectric response for cutaneous pressure monitoring. *Nat. Commun.* **5**, 4496 (2014).
7. Liu, X. et al. BaTiO<sub>3</sub>/MXene/PVDF-TrFE composite films via an electrospinning method for flexible piezoelectric pressure sensors. *J. Mater. Chem. C.* **11**, 4614–4622 (2023).
8. Jiang, X., Kim, K., Zhang, S., Johnson, J. & Salazar, G. High-temperature piezoelectric sensing. *Sensors* **14**, 144–169 (2014).
9. Zu, H., Wu, H. & Wang, Q.-M. High-temperature piezoelectric crystals for acoustic wave sensor applications. *IEEE Trans. Ultrason., Ferroelectr., Frequency Control* **63**, 486–505 (2016).
10. Li, F. et al. Ultrahigh piezoelectricity in ferroelectric ceramics by design. *Nat. Mater.* **17**, 349–354 (2018).
11. Lee, Y. et al. Flexible ferroelectric sensors with ultrahigh pressure sensitivity and linear response over exceptionally broad pressure range. *ACS Nano* **12**, 4045–4054 (2018).
12. Huang, Y. et al. Enhanced piezoelectricity from highly polarizable oriented amorphous fractions in biaxially oriented poly(vinylidene fluoride) with pure  $\beta$  crystals. *Nat. Commun.* **12**, 675 (2021).
13. Liao, W.-Q. et al. A molecular perovskite solid solution with piezoelectricity stronger than lead zirconate titanate. *Science* **363**, 1206–1210 (2019).
14. He, J. et al. A Universal high accuracy wearable pulse monitoring system via high sensitivity and large linearity graphene pressure sensor. *Nano Energy* **59**, 422–433 (2019).
15. Lin, M.-F., Cheng, C., Yang, C.-C., Hsiao, W.-T. & Yang, C.-R. A wearable and highly sensitive capacitive pressure sensor integrated a dual-layer dielectric layer of PDMS microcylinder array and PVDF electrospun fiber. *Org. Electron.* **98**, 106290 (2021).
16. Jin, C. et al. A wearable combined wrist pulse measurement system using airbags for pressurization. *Sensors* **19**, 386 (2019).
17. Bijender & Kumar, S. Flexible and wearable capacitive pressure sensor for blood pressure monitoring. *Sens. Bio-Sens. Res.* **33**, 100434 (2021).
18. Wang, X., Liu, Z. & Zhang, T. Flexible sensing electronics for wearable/attachable health monitoring. *Small* **13**, 1602790 (2017).
19. Pang, Y. et al. Flexible, highly sensitive, and wearable pressure and strain sensors with graphene porous network structure. *ACS Appl. Mater. Interfaces* **5**, 26458–26462 (2016).
20. Gao, C., Long, Z., Zhong, T., Liang, S. & Xing, L. A self-powered intelligent glove for real-time human-machine gesture interaction based on piezoelectric effect of T-ZnO/PVDF film. *J. Phys. D: Appl. Phys.* **55**, 194004 (2022).
21. Self-powered, high sensitivity printed e-tattoo sensor for unobtrusive arterial pulse wave monitoring. *Nano Energy* **102**, 107625 (2022).
22. Hao, Z. & Wang, D. Arterial pulse signal amplification by adding a uniform PDMS layer to a pyrex-based microfluidic tactile sensor. *IEEE Sens. J.* **20**, 2164–2172 (2020).
23. Park, D. Y. et al. Self-powered real-time arterial pulse monitoring using ultrathin epidermal piezoelectric sensors. *Adv. Mater.* **29**, 1702308 (2017).
24. Boutry, C. M. et al. Biodegradable and flexible arterial-pulse sensor for the wireless monitoring of blood flow. *Nat. Biomed. Eng.* **3**, 47–57 (2019).
25. Yang, Y. et al. Breathable electronic skins for daily physiological signal monitoring. *Nano-Micro Lett.* **14**, 161 (2022).
26. Liu, D. et al. Intrinsically stretchable polymer semiconductor based electronic skin for multiple perceptions of force, temperature, and visible light. *Nano Res* **16**, 1196–1204 (2023).
27. Duan, S. et al. Water-modulated biomimetic hyper-attribute-gel electronic skin for robotics and skin-attachable wearables. *ACS Nano* **17**, 1355–1371 (2023).
28. Wang, Y., Hong, M., Venezuela, J., Liu, T. & Dargusch, M. Expedient secondary functions of flexible piezoelectrics for biomedical energy harvesting. *Bioact. Mater.* **22**, 291–311 (2023).
29. Kim, M. & Yun, K.-S. Helical piezoelectric energy harvester and its application to energy harvesting garments. *Micromachines* **8**, 115 (2017).
30. Hu, N. et al. Stretchable kirigami polyvinylidene difluoride thin films for energy harvesting: design, analysis, and performance. *Phys. Rev. Appl.* **9**, 021002 (2018).
31. Zhou, H. et al. Stretchable piezoelectric energy harvesters and self-powered sensors for wearable and implantable devices. *Biosens. Bioelectron.* **168**, 112569 (2020).
32. Su, Y. et al. Muscle fibers inspired high-performance piezoelectric textiles for wearable physiological monitoring. *Adv. Funct. Mater.* **31**, 2010962 (2021).
33. Lin, W. et al. Skin-inspired piezoelectric tactile sensor array with crosstalk-free Row+Column electrodes for spatiotemporally distinguishing diverse stimuli. *Adv. Sci.* **8**, 2002817 (2021).
34. Abdul Razak, A. H., Zayegh, A., Begg, R. K. & Wahab, Y. Foot plantar pressure measurement system: A review. *Sensors* **12**, 9884–9912 (2012).
35. Urry, S. Plantar pressure-measurement sensors. *Meas. Sci. Technol.* **10**, R16 (1999).
36. Meng, K. et al. Wearable pressure sensors for pulse wave monitoring. *Adv. Mater.* **34**, 2109357 (2022).
37. Gad-el-Hak, M. *The MEMS Handbook*. (CRC Press, 2001).
38. Kong, H., Jin, Y., Li, G., Zhang, M. & Du, J. Design and Fabrication of a Hierarchical Structured Pressure Sensor Based on BaTiO<sub>3</sub>/PVDF Nanofibers via Near-Field Electrospinning. *Adv. Eng. Mater.* 2201660 <https://doi.org/10.1002/adem.202201660> (2023)
39. Yang, Y. et al. Flexible piezoelectric pressure sensor based on polydopamine-modified BaTiO<sub>3</sub>/PVDF composite film for human motion monitoring. *Sens. Actuat. A-Phys.* **301**, 111789 (2020).
40. Chen, X. et al. High-performance piezoelectric nanogenerators with imprinted P(VDF-TrFE)/BaTiO<sub>3</sub> nanocomposite micropillars for self-powered flexible sensors. *Small* **13**, 1604245 (2017).
41. Yang, C.-R. et al. Highly sensitive and wearable capacitive pressure sensors based on PVDF/BaTiO<sub>3</sub> composite fibers on PDMS microcylindrical structures. *Measurement* **202**, 111817 (2022).

42. Singh, H. H., Singh, S. & Khare, N. Design of flexible PVDF/NaNbO<sub>3</sub>/RGO nanogenerator and understanding the role of nanofillers in the output voltage signal. *Compos. Sci. Technol.* **149**, 127–133 (2017).
43. Deng, W. et al. Cowpea-structured PVDF/ZnO nanofibers based flexible self-powered piezoelectric bending motion sensor towards remote control of gestures. *Nano Energy* **55**, 516–525 (2019).
44. Bhatt, A. et al. Enhanced piezoelectric response using TiO<sub>2</sub>/MoS<sub>2</sub> heterostructure nanofillers in PVDF based nanogenerators. *J. Alloy. Compd.* **960**, 170664 (2023).
45. Li, S., Zhang, M., Sun, J., Sun, J. & Wang, Y. Preparation and characterization of superior hydrophilic PVDF/DA membranes by the self-polymerization approach of dopamine. *Front. Chem.* **11**, 1162348 (2023).
46. Pang, C. et al. Highly skin-conformal microhairy sensor for pulse signal amplification. *Adv. Mater.* **27**, 634–640 (2015).
47. Kim, Y., Lee, J., Hong, H., Park, S. & Ryu, W. Self-Powered Wearable Micropyramid Piezoelectric Film Sensor for Real-Time Monitoring of Blood Pressure. *Adv. Eng. Mater.* 2200873 <https://doi.org/10.1002/adem.202200873> (2022).
48. Song, J. et al. Stretchable Strain and Strain Rate Sensor Using Kirigami-Cut PVDF Film. *Adv. Mater. Technol.* 2201112 <https://doi.org/10.1002/admt.202201112> (2023).
49. Meng, K. et al. Kirigami-inspired pressure sensors for wearable dynamic cardiovascular monitoring. *Adv. Mater.* **34**, 2202478 (2022).
50. Kim, Y.-G., Song, J.-H., Hong, S. & Ahn, S.-H. Piezoelectric strain sensor with high sensitivity and high stretchability based on kirigami design cutting. *npj Flex. Electron.* **6**, 52 (2022).
51. Zhang, Y. et al. A mechanically driven form of Kirigami as a route to 3D mesostructures in micro/nanomembranes. *Proc. Natl Acad. Sci. USA* **112**, 11757–11764 (2015).
52. Han, M. et al. Three-dimensional piezoelectric polymer microsystems for vibrational energy harvesting, robotic interfaces and biomedical implants. *Nat. Electron.* **2**, 26–35 (2019).
53. Cheng, X. et al. Bioinspired design and assembly of a multilayer cage-shaped sensor capable of multistage load bearing and collapse prevention. *Nanotechnology* **32**, 155506 (2021).
54. Wang, J. et al. Diaphragm-based optical fiber sensor for pulse wave monitoring and cardiovascular diseases diagnosis. *J. Biophotonics* **12**, e201900084 (2019).
55. Janjua, G. M. W., Finlay, D., Guldenring, D., Haq, A. U. & McLaughlin, J. Evaluation of pulse transit time for different sensing methodologies of arterial waveforms. *IEEE Access* **11**, 33928–33933 (2023).
56. Kil, H.-J. & Park, J.-W. Carotid artery monitoring patch using a supercapacitive pressure sensor with piezoelectricity. *Nano Energy* **114**, 108636 (2023).
57. Luo, N. et al. Flexible piezoresistive sensor patch enabling ultralow power cuffless blood pressure measurement. *Adv. Funct. Mater.* **26**, 1178–1187 (2016).
58. Chiu, Y.-Y., Lin, W.-Y., Wang, H.-Y., Huang, S.-B. & Wu, M.-H. Development of a piezoelectric polyvinylidene fluoride (PVDF) polymer-based sensor patch for simultaneous heartbeat and respiration monitoring. *Sens. Actuat. A-Phys.* **189**, 328–334 (2013).
59. Marechal, L. et al. Toward a common framework and database of materials for soft robotics. *Soft Robot.* **8**, 284–297 (2020).

## Acknowledgements

This work is supported by the National Natural Science Foundation of China (NSFC) (62004009 for C. L.), the National Key Research and Development Program of China (Grant No. 2018YFA0702100), the Zhejiang Provincial Key Research and Development Program of China (Grant Nos. 2021C01026 and 2021C05002), the Leading Innovative and Entrepreneur Team Introduction Program of Zhejiang (2020R01007) and Beijing Nova Program (20230484412).

## Author contributions

C.L. developed the concepts. Y.Z. performed device fabrication. Y.Z., D.M., B.J., X.T. and Y.C. performed device characterization. Y.Z. analyzed the experimental data. Y.Z. performed simulations. C.L. and Y.D. provided funding support. C.L. and Y.Z. wrote the manuscript.

## Competing interests

The authors declare no competing interests.

## Informed consent

Written informed consent has been obtained from all the participant.

## Additional information

**Supplementary information** The online version contains supplementary material available at <https://doi.org/10.1038/s41528-024-00310-6>.

**Correspondence** and requests for materials should be addressed to Changbo Liu or Yuan Deng.

**Reprints and permissions information** is available at <http://www.nature.com/reprints>

**Publisher's note** Springer Nature remains neutral with regard to jurisdictional claims in published maps and institutional affiliations.

**Open Access** This article is licensed under a Creative Commons Attribution 4.0 International License, which permits use, sharing, adaptation, distribution and reproduction in any medium or format, as long as you give appropriate credit to the original author(s) and the source, provide a link to the Creative Commons licence, and indicate if changes were made. The images or other third party material in this article are included in the article's Creative Commons licence, unless indicated otherwise in a credit line to the material. If material is not included in the article's Creative Commons licence and your intended use is not permitted by statutory regulation or exceeds the permitted use, you will need to obtain permission directly from the copyright holder. To view a copy of this licence, visit <http://creativecommons.org/licenses/by/4.0/>.

© The Author(s) 2024